UCLA

Title

On the forward modeling of radar Doppler spectrum width from LES: Implications for model evaluation.

Permalink

Journal

ISSN

Authors

Chen, Y-S
Verlinde, J
Clothiaux, E
et al.

Publication Date

DOI

On the forward modeling of radar Doppler spectrum width from LES: Implications for model evaluation

Y.-S. Chen[1], **J. Verlinde**[1], **E. E. Clothiaux**[1], **A. S. Ackerman**[2], **A. M. Fridlind**[2], **M. Chamecki**[3], **P. Kollias**[4,5], **M. P. Kirkpatrick**[6], **B.-C. Chen**[1], **G. Yu**[1,*], and **A. Avramov**[2,†]

[1]Department of Meteorology and Atmospheric Science, The Pennsylvania State University, University Park, PA

[2]NASA Goddard Institute for Space Studies, New York, NY

[3]Department of Atmospheric and Oceanic Sciences, University of California, Los Angeles, Los Angeles, California

[4]School of Marine and Atmospheric Sciences, Stony Brook University, Stony Brook, NY

[5]Environmental and Climate Sciences Department, Brookhaven National Laboratory, Upton, NY

[6]School of Aerospace, Mechanical and Mechatronic Engineering, The University of Sydney

Abstract

Large-eddy simulations of an observed single-layer Arctic mixed-phase cloud are analyzed to study the value of forward modeling of profiling millimeter-wave cloud radar Doppler spectral width for model evaluation. Individual broadening terms and their uncertainties are quantified for the observed spectral width and compared to modeled broadening terms. Modeled turbulent broadening is narrower than the observed values when the turbulent kinetic energy dissipation rate from the subgrid-scale model is used in the forward model. The total dissipation rates, estimated with the subgrid-scale dissipation rates and the numerical dissipation rates, agree much better with both the retrieved dissipation rates and those inferred from the power spectra of the simulated vertical air velocity. The comparison of the microphysical broadening provides another evaluative measure of the ice properties in the simulation. To accurately retrieve dissipation rates as well as each broadening term from the observations, we suggest a few modifications to previously presented techniques. First, we show that the inertial subrange spectra filtered with the radar sampling volume is a better underlying model than the unfiltered −5/3 law for the retrieval of the dissipation rate from the power spectra of the mean Doppler velocity. Second, we demonstrate that it is important to filter out turbulence and remove the layer-mean reflectivity-weighted mean fall speed from the observed mean Doppler velocity to avoid overestimation of shear broadening. Finally, we provide a method to quantify the uncertainty in the retrieved dissipation rates, which eventually propagates to the uncertainty in the microphysical broadening.

Corresponding Author: Y.-S. Chen (yxc255@psu.edu).
*Current Affiliation: Compagnie Générale de Géophysique, Houston, TX
†Current Affiliation: Department of Environmental Sciences, Emory University, Atlanta, GA

1. Introduction

Mixed-phase clouds are ubiquitous in the Arctic boundary layer [Curry et al., 1996; Intrieri et al., 2002; Shupe et al., 2006; Shupe, 2011]. They are critical to the shortwave and longwave radiative budgets of the Arctic and linked to sea ice and ice sheet melt and Arctic air mass formation [Kay et al., 2008; Sedlar et al., 2011; Persson et al., 2017]. The properties of Arctic mixed-phase clouds are determined by the complicated interactions between various physical processes including turbulence and microphysical processes [Morrison et al. 2012]. To improve large-eddy simulations (LES) for these clouds, it is necessary to evaluate model performance in capturing both turbulent air motions and microphysical characteristics of the hydrometeors, dependent, in part, on model assumptions regarding ice particle fall speeds, morphologies, and densities.

The profiling millimeter-wave cloud radar (MMCR) [*Moran et al.*, 1998; Kollias et al., 2007] has been deployed at the Department of Energy (DOE) Atmospheric Radiation Measurement (ARM) Climate Research Facility (CRF) located on the North Slope of Alaska (NSA) near Barrow to provide observations of Arctic mixed-phase clouds [Shupe et al., 2008a; Rambukkange et al., 2011]. A Doppler spectrum reported by these radars can be interpreted as the distribution of the scatterers' reflectivity versus their vertical velocity. The radar sampling volume acts as a spatial and temporal filter of the particle motion. If the scatterers are "ideal", that is, move at the same velocity as the air, are uniformly distributed in space, and have constant backscattering cross section, the filter characteristics are determined by both the configuration of the radar and the horizontal wind speed. (See White et al. [1999] for details.) The mean Doppler velocity is then the filtered vertical air velocity v_a. For these ideal scatterers the squared Doppler spectral width σ_{dyn}^2 is the variance of the residual vertical air velocity within the radar samplingvolume with contributions from turbulent air motions (σ_t^2) and the gradient of mean air velocity, which we refer to as the shear broadening (σ_s^2) following the convention in the radar meteorologycommunity, as well as the projection of the horizontal wind speed in the radial direction due to finite radar beam width (σ_{bw}^2). For Doppler spectral widths estimated for an individual radar volume there may be correlations between these mechanisms [Fang and Doviak, 2008; Fang et al., 2011]. However, in expectation these correlation terms between mechanisms vanish and

$$\sigma_{dyn}^2 = \sigma_t^2 + \sigma_s^2 + \sigma_{bw}^2. \quad (1)$$

The subscript "dyn" indicates that in this case the Doppler spectrum is only broadened by dynamical factors. For real particles, the mean Doppler velocity v_d is the filtered vertical air velocity v_a (defined as positive upwards) minus the reflectivity-weighted mean fall speed of the particles v_f, and the squared Doppler spectral width σ^2 is the variance of the residual vertical air velocity plus microphysical broadening σ_{mp}^2, that is, the variance contributed by the distribution of particle reflectivities as a function of particle fall speed [Doviak and Zrni , 1993]:

$$v_d = v_a - v_f, \quad (2)$$

$$\sigma^2 = \sigma_{mp}^2 + \sigma_{dyn}^2 = \sigma_{mp}^2 + \sigma_t^2 + \sigma_s^2 + \sigma_{bw}^2. \quad (3)$$

The connection between Doppler spectra and atmospheric dynamics and microphysics provides the basis for the forward models that predict the Doppler spectra or their moments using cloud properties from an LES. Thus, the model performance can be evaluated through the comparison between the modeled and observed Doppler spectra and their moments, i.e., the reflectivity, the mean Doppler velocity, and the Doppler spectral width. One can also retrieve physical quantities from radar observations and compare them with their counterparts from numerical simulations. Borque et al. [2016] developed a method to partition the observed spectral width into contributions from various mechanisms with a few steps. First, retrieve the turbulent kinetic energy dissipation rate, referred to as the dissipation rate for short, from the time series of the mean Doppler velocity. Then, calculate the turbulent broadening from the retrieved dissipation rates. Third, estimate the shear broadening from the observed mean Doppler velocity. Finally, microphysical broadening is what remains after removal of these broadening terms as well as the often small beam width effect.

The Distributed Hydrodynamic Aerosol and Radiative Modeling Application (DHARMA) model was used to simulate a single-layer, mixed-phase cloud observed on April 8, 2008, during the Indirect and Semi-Direct Aerosol Campaign (ISDAC) [McFarquhar et al., 2011] at the NSA site [Avramov et al., 2011]. The goal of the simulations was to test model assumptions regarding both ice nucleation and ice particle properties. While a few model configurations were found to produce simulations in good agreement with in situ measurements and the reflectivity and mean Doppler velocity from the MMCR deployed at NSA, Avramov et al. [2011] briefly noted that modeled spectral widths (in m s^{-1}) were roughly a factor of two narrower than observed.

We are motivated to explore the spectral width because it is a useful quantity for at least two reasons. First, the spectral width provides information on both dynamics and microphysics. Traditional techniques using Doppler radar moments for the retrieval of atmospheric dynamics and microphysics typically prescribe the turbulent contribution to the spectral width [e.g., Deng and Mace, 2006]. With the recent work by Borque et al. [2016], spectral width's dynamical and microphysical broadening components were separately retrieved. Evaluation of model microphysics with retrieved microphysical broadening terms with known uncertainties would facilitate making fewer additional assumptions about the observations. Second, interest in higher moments like skewness and kurtosis is growing [Kollias et al., 2011a, 2011b; Maahn et al., 2015, 2017; Rémillard et al., 2017]. Assuming the dynamical factors broaden the Doppler spectra in a Gaussian manner, the deviations between modeled or observed skewness and kurtosis from those expected from a Gaussian distribution contain information on the microphysics. In other words, interpretation of

skewness and kurtosis of the Doppler spectra requires an accurate estimation of the dynamical broadening, and a good representation of the dynamical broadening is required to make meaningful comparisons of skewness and kurtosis between modeled Doppler spectra and observed ones [Kollias et al., 2011a].

In this study, we extend the evaluation by Avramov et al. [2011] to focus on the Doppler spectral width. We decompose the dynamical and microphysical broadening in observed Doppler spectral widths following the general steps reported in Borque et al. [2016] but with a few modifications. Then, we compare the observed dynamical and microphysical broadening separately with those modeled based on DHARMA simulations. We briefly introduce the theoretical background for the method in Section 2, introduce the case and DHARMA simulation results in Section 3, report our spectral width decomposition method as well as the results from each step in Section 4, and discuss turbulent broadening, microphysical broadening, and implications of the study in Section 5.

2. Filtering turbulent flow

In this section, we introduce the necessary background for our methods in Sections 3 and 4 based in part on Chapters 6 and 11 in Pope [2000] and Chapter 10 in Doviak and Zrni [1993]. Elements of our approach include: (1) one-dimensional power spectra of the vertical air velocity unfiltered or filtered by radar sampling volume or LES model filter, and (2) the residual vertical air velocity variance as a function of the filter characteristics and the dissipation rate. In what follows subscript 1 indicates the x-direction or the direction along the horizontal mean wind, subscript 2 indicates the y-direction or the horizontal direction transverse to the horizontal mean wind, and subscript 3 indicates the z-direction or vertical direction.

Consider some stationary flow where the kinetic energy density for vertical air velocity is proportional to $\Phi_{33}(\boldsymbol{\kappa})$, one component of the velocity-spectrum tensor, where $\boldsymbol{\kappa}$ is the three-dimensional wavenumber vector. For homogeneous and isotropic turbulent flow, $\Phi_{33}(\boldsymbol{\kappa})$ has the form

$$\Phi_{33}(\boldsymbol{\kappa}) = \frac{E(\kappa)}{4\pi\kappa^2}\left(1 - \frac{\kappa_3^2}{\kappa^2}\right), \quad (4)$$

with κ representing the magnitude of $\boldsymbol{\kappa}$. For the inertial subrange of the turbulent flow, (κ) is the Kolmogorov power spectrum

$$E(\kappa) = C\epsilon^{2/3}\kappa^{-5/3}, \quad (5)$$

where C is the Kolmogorov constant of 1.5 and ϵ is the turbulent kinetic energy dissipation rate. The one-dimensional power spectrum of the vertical air velocity versus the wavenumber along the direction of the horizontal mean wind is obtained by the following integrals of the corresponding velocity-spectrum tensors:

$$E_{33}(\kappa_1) = 2 \int_{-\infty}^{\infty} \int_{-\infty}^{\infty} \Phi_{33}(\boldsymbol{\kappa}) d\kappa_2 d\kappa_3, \quad (6)$$

There is a wavenumber range where $E_{33}(\kappa_1)$ follows a $-5/3$ law:

$$E_{33}(\kappa_1) = C_1' \epsilon^{2/3} \kappa_1^{-5/3} \approx 0.65 \epsilon^{2/3} \kappa_1^{-5/3}. \quad (7)$$

One can also define a one-dimensional power spectrum of the vertical air velocity versus the horizontal wavenumber $\kappa_h = \sqrt{\kappa_1^2 + \kappa_2^2}$, $E_{33}(\kappa_h)$, by taking the integral of $\Phi_{33}(\boldsymbol{\kappa})$ with respect to κ_h.

If a filter with transfer function $\hat{G}(\boldsymbol{\kappa})$ is applied to the flow, the filtered velocity-spectrum tensor for vertical air velocity is

$$\widetilde{\Phi}_{33}(\boldsymbol{\kappa}) = \left| \hat{G}(\boldsymbol{\kappa}) \right|^2 \Phi_{33}(\boldsymbol{\kappa}), \quad (8)$$

where we use a tilde to indicate a filtered quantity. The one-dimensional power spectra of the filtered vertical air velocity versus κ_1 and κ_h, denoted $\tilde{E}_{33}(\kappa_1)$ and $\tilde{E}_{33}(\kappa_h)$, are similarly defined as their unfiltered counterparts, but with $\Phi_{33}(\boldsymbol{\kappa})$ in their integration replaced with $\widetilde{\Phi}_{33}(\boldsymbol{\kappa})$. For example,

$$\tilde{E}_{33}(\kappa_1) = 2 \int_{-\infty}^{\infty} \int_{-\infty}^{\infty} \widetilde{\Phi}_{33}(\boldsymbol{\kappa}) d\kappa_2 d\kappa_3 = 2 \int_{-\infty}^{\infty} \int_{-\infty}^{\infty} \left| \hat{G}(\boldsymbol{\kappa}) \right|^2 \Phi_{33}(\boldsymbol{\kappa}) d\kappa_2 d\kappa_3. \quad (9)$$

The residual vertical air velocity variance is

$$\sigma_r^2 = \int_{-\infty}^{\infty} \int_{-\infty}^{\infty} \int_{-\infty}^{\infty} \left(1 - \left| \hat{G}(\boldsymbol{\kappa}) \right|^2 \right) \Phi_{33}(\boldsymbol{\kappa}) d\kappa_1 d\kappa_2 d\kappa_3. \quad (10)$$

If the characteristic width of the filter falls in the inertial subrange, and the homogeneous and isotropic turbulence dominates the residual vertical air velocity variance, with Eqs. (4) and (5), this variance is proportional to $\epsilon^{2/3}$.

The sampling volume of a vertically pointing Doppler radar filters the air motion both spatially and temporally [White et al., 1999]. For the rest of this study, we define the squared transfer function for radar sampling volumes at range z of a profiling Doppler radar with narrow beam width θ, pulse width τ, and dwell time T as

$$\left|\hat{G}(\boldsymbol{\kappa})\right|^2 = \exp\left\{-\left[\frac{z^2\theta^2}{16\log(2)} + \frac{U^2(z)T^2}{12}\right]\kappa_1^2 - \frac{z^2\theta^2}{16\log(2)}\kappa_2^2 - (0.35c\tau)^2\kappa_3^2\right\}. \quad (11)$$

In this equation c is the speed of light and (z) is the speed of the horizontal wind at range z. Both the range weighting function and the advection by the horizontal wind are treated as Gaussian patterns. This equation is the same as the one used in the integration in Eq. (2.14) in White et al. [1999], except that the impact of the horizontal wind is approximated with a Gaussian function as discussed in Section 3c of White et al. [1999].

The spatial and temporal filtering by the profiling Doppler radar sampling volume modifies the one-dimensional power spectrum of the vertical air velocity $E_{33}(\kappa_1)$, resulting in the filtered power spectrum, or the power spectrum of the filtered vertical air velocity $\tilde{E}_{33}(\kappa_1)$. We define functions $C_{33}(\kappa_1)$ and $\tilde{C}_{33}(\kappa_1)$ so that

$$E_{33}(\kappa_1) = C_{33}(\kappa_1)\epsilon^{2/3}, \quad (12)$$

$$\tilde{E}_{33}(\kappa_1) = \tilde{C}_{33}(\kappa_1)\epsilon^{2/3}. \quad (13)$$

3. Case study observations and DHARMA simulations

A single-layer mixed-phase cloud was observed at the ARM NSA site near Barrow, Alaska, on April 8, 2008, during ISDAC. Figure 1 shows an overview of the case based on the observations from the MMCR, the best estimate of the liquid water path [Turner et al., 2007], and the liquid cloud base reported by a ceilometer. DHARMA was used to simulate this case [Avramov et al., 2011] with the goal of testing whether good agreement between observations and simulations could be achieved if ice nucleation is constrained with measured heterogeneous ice nuclei concentrations. DHARMA consists of an LES dynamical core [Stevens et al., 2002] with a dynamic Smagorinsky subgrid-scale (SGS) model [Kirkpatrick et al., 2006], coupled with a size resolved bin microphysics model [Ackerman et al., 1995, 2004; Fridlind et al., 2007] and a two-stream radiative transfer model [Toon et al., 1989]. In this study, we focus on two simulations reported by Avramov et al. [2011]. Both simulations included dendritic pristine ice and aggregates of dendrites, referred to as "dendrites" and "aggregates" hereafter, with one using properties of low-density dendrites with stellar arms and their aggregates (LOW) and the other using properties of high-density dendrites represented as thin plates and their aggregates (HIGH), intended to bound the wide range of dendrite density established from in situ images (see Fig. 4 of Avramov et al. [2011]). In DHARMA, the specified ice particle mass, maximum dimension, projected area and aspect ratio are used in a physically consistent manner to calculate the ice particle properties, such as fall speed (Fig. 2a) and particle reflectivity (Fig. 2b). The primary difference in particle fall speeds is that for sizes larger than approximately 100 μm,

aggregates in HIGH fall faster than in LOW, whereas ice particles smaller than approximately 100 μm fall with the same speeds. The size-dependent particle reflectivity is calculated to match the DHARMA ice particle assumptions by Botta et al. [2011] and is the same as that used by Avramov et al. [2011].

To investigate the spectral width, we analyze the three-dimensional outputs from both LOW and HIGH simulations at 4, 4.5, 5, 5.5, and 6 h from the beginning of the simulation and compare them with the observations from 17:00 UTC to 17:30 UTC, April 8, 2008. The short period of observations is used because the simulation is initialized with the sounding from a radiosonde launched around 17:30 UTC and the observations during this half-hour period showed relatively stationary characteristics; conclusions are not sensitive to using observations from the half hour prior or later. The Doppler spectra are calculated for every model grid box using the forward model described in Appendix A. The rate of kinetic energy transfer between resolved and subgrid scales computed with the eddy viscosity from the SGS model, hereafter the "SGS dissipation rate", is used to calculate the turbulent broadening in the forward model. The reflectivity, the mean Doppler velocity, and the Doppler spectral width are calculated from the modeled Doppler spectra.

We confirm previous evaluation results that the LOW simulation produce the reflectivities in very good agreement with the observations but the HIGH simulation underestimate the reflectivities (Fig. 3a). Although both simulations produce frequency of occurrence histograms of mean Doppler velocities that are similar to the observations (not shown), the layer mean values from both LOW and HIGH simulations are slower than the observations (Fig. 3b). (The significance of this discrepancy will be discussed later with our analysis of the spectral widths.) We also find that both simulations produce typical spectral widths that are substantially narrower than those observed (Fig. 3c), as noted but not shown in Avramov et al. [2011]. For the bulk of the liquid cloud, the layer-mean of the modeled squared spectral widths are around 0.01 m^2 s^{-2} for the LOW simulation and around 0.02 m^2 s^{-2} for the HIGH simulation, while those observed are close to 0.05 m^2 s^{-2}. When converted to spectral width, these valuesare comparable to the numbers reported by Avramov et al. [2011], i.e., $\sim$0.1 m s^{-1} for the modeled spectra and $\sim$0.2 m s^{-1} for the observations. These results hold true for all five time slices from the LOW and HIGH simulations. The mean observed liquid water path during the selected time is 40.8 g m^{-2}, while the LOW and HIGH simulations produce 34.7 g m^{-2} and 36.7 g m^{-2}, respectively. (Note that the location of the simulated liquid-cloud top in the modeldomain is lower by around 50 m than the highest height of observed significant radar return. All profiles for the simulations are shifted up for 50 m to compensate for this difference.)

Figure 4 shows the normalized frequency of occurrence of the observed (squared) Doppler spectral widths and those modeled based on the simulation results at 4 h. The observed Doppler spectra become slightly wider away from the liquid-cloud top and then stay approximately constant throughout the rest of the liquid-cloud layer. The Doppler spectral widths produced from the LOW simulation also widen just below liquid-cloud top, but then narrow again down towards the liquid-cloud base. The Doppler spectral widths produced from the HIGH simulation exhibit a height dependence more comparable to the observations.

4. Comparison of simulation outputs to observations

In this section, we retrieve the turbulent kinetic energy dissipation rates from the observed mean Doppler velocity to evaluate the SGS dissipation rates from DHARMA. Then we decompose the observed Doppler spectral widths into individual broadening terms and focus our evaluation on the microphysical broadening.

4.1. Dissipation rates and turbulent broadening

We first detrended the observed mean Doppler velocity series for each range gate by applying a Gaussian filter with a filter width of 1.5 km, removed the filtered velocity and kept only the residual velocity. We then removed the remaining linear trend in the residual time series. The autocorrelation of the detrended series was subsequently shown to have the expected behavior of a turbulent velocity time series (i.e., the autocorrelation falls to below zero as the lag initially increases, then returns to positive values and then oscillates around zero). We next calculated the power spectra of the detrended observed mean Doppler velocity time series, $E_{33}^{\mathrm{obs}}(\kappa_1)$, from 17:00 UTC to 17:30 UTC at each range gate height. Then we smoothed $E_{33}^{\mathrm{obs}}(\kappa_1)$ by averaging them over non-overlapping wavenumber ranges with similar widths in log scale following Section 7.4.1 in Kaimal and Finnigan [1994], and visually examined the smoothed power spectra for inertial subrange behavior. Retrieval of the dissipation rates was attempted for heights where the smoothed power spectra showed an approximate −5/3 slope. Figure 5a show the smoothed $E_{33}^{\mathrm{obs}}(\kappa_1)$ at various heights. One can see that the power spectra inthe lower part of the liquid cloud show approximately −5/3 slopes. The inertial subrange behavior collapses as one moves towards the liquid cloud top, possibly because the outer length scale of the homogeneous and isotropic turbulence gets smaller so that filtering by the radar sampling volume distorts the −5/3 spectra too much. We chose to retrieve the dissipation rate for four heights between 800 m and 1000 m.

For each of these four heights, we numerically calculated $C_{33}(\kappa_1)$ and $\tilde{C}_{33}(\kappa_1)$ for the same wavenumber points as $E_{33}^{\mathrm{obs}}(\kappa_1)$ assuming the Kolmogorov spectrum. The highest resolvable wavenumber is $\kappa_0 = \frac{\pi}{U\Delta t}$, where $t \approx 3.08$ s is the time interval between MMCR profiles and U is the horizontal wind speed obtained by interpolating observed radiosonde wind speeds to the heights of the range gate. (Note that the height dependence is dropped in the notation.) The spectral power beyond the highest resolvable wavenumber is not lost but aliased back to the resolved wavenumber points. The aliased versions of $C_{33}(\kappa_1)$ and $\tilde{C}_{33}(\kappa_1)$, called $C_{33}^{\mathrm{a}}(\kappa_1)$ and $\tilde{C}_{33}^{\mathrm{a}}(\kappa_1)$, are also calculated for the same wavenumber points as $E_{33}^{\mathrm{obs}}(\kappa_1)$. We further estimated the integral length scale L from the autocorrelation function of the detrended observed mean Doppler velocity time series at each height. Then we computed four dissipation rates following

$$\epsilon = \left(\frac{\sum_{\kappa_1} E_{33}^{\text{obs}}(\kappa_1)}{\sum_{\kappa_1} C_{33}^{\text{model}}(\kappa_1)} \right)^{3/2}, \frac{2\pi}{L} < \kappa_1 < \kappa_0, \quad (14)$$

where $C_{33}^{\text{model}}(\kappa_1)$ is one of the four possible underlying models $C_{33}(\kappa_1)$, $\tilde{C}_{33}(\kappa_1)$, $C_{33}^{\text{a}}(\kappa_1)$, and $\tilde{C}_{33}^{\text{a}}(\kappa_1)$. We assumed no white noise contribution in $E_{33}^{\text{obs}}(\kappa_1)$ to obtain an upper bound on the dissipation rates. Note that we are fitting the underlying models for turbulent air motion to power spectra obtained from mean Doppler velocities, which are filtered vertical air velocities v_{a} (defined as positive upwards) minus the reflectivity-weighted mean fall speed of the particles v_{f}. Both the variance of v_{f} and the covariance between v_{f} and v_{a} can bias $E_{33}^{\text{obs}}(\kappa_1)$ relative to the desired power spectra of v_{a}. We follow Lothon et al. [2005] who showed that the variance of v_{f} is much smaller than that of v_{a} and the covariance between v_{f} and v_{a} mostly occurs at larger scales.

Figure 5b shows an example for the range gate at 870.2 m. The retrieved power spectra for all four underlying models are shown. The observed spectrum shows deviations from the −5/3 behavior that requires filtering by the radar sampling volume to explain. The sum of $\tilde{C}_{33}(\kappa_1)$ is the smallest among the four underlying models. Therefore, the retrieved dissipation rate assuming $\tilde{C}_{33}(\kappa_1)$ is the largest of the four underlying models. For the four heights wherewe applied the retrieval, the dissipation rates based on $\tilde{C}_{33}(\kappa_1)$ are about 167%~182% of the results based on $C_{33}(\kappa_1)$. We also examined which of the four underlying models produces thebest fit to the observed spectra, finding no evidence of aliasing present in them. Therefore, we selected the filtered inertial subrange spectra without aliasing, i.e., $\tilde{C}_{33}(\kappa_1)$, for our retrievals.

We quantify the uncertainty in the retrieved dissipation rates following methods similar to O'Connor et al. [2010] and Shupe et al. [2012]. With a fixed underlying model, the fractional error in the dissipation rate is defined as the sum of two terms, that is,

$$\frac{\Delta \epsilon}{\epsilon} = \frac{3}{2} \frac{\Delta \sigma_{\text{i}}^2}{\sigma_{\text{i}}^2} + \frac{\Delta U}{U}, \quad (15)$$

where σ_{i}^2 is the expected integral of the power between the wavenumber range $\frac{2\pi}{L} < \kappa_1 < \kappa_0$, $\Delta \sigma_{\text{i}}^2$ is the error in the estimation of σ_{i}^2, and $\frac{\Delta U}{U}$ is the fractional error in the horizontal wind speed. To estimate the uncertainty in σ_{i}^2, we assume that the ratio between the observed powerdensity $E_{33}^{\text{obs}}(\kappa_1)$ and the expected power density, denoted with $E_{33}^{\text{exp}}(\kappa_1)$, is a random variablefollowing the exponential distribution with a parameter of 1 and independent of the ratio at other wavenumbers. This assumed distribution is consistent with

that, at each wavenumber point, the variance of the power density is the square of the expected power density [Appendix B in Fang et al., 2011; Dias 2017]. This assumption also empirically matches the observed spectra. Under this assumption, the integrated power is the sum of a number of random variables following a Gamma distribution. We generated 10^5 random spectra based on each of the four underlying models at the same wavenumber points used to retrieve the dissipation rate. The ratio between the standard deviation of the integral of the randomly generated power spectra and the true value vary from about 7.5% to 10.0% across the four underlying models. This experiment was repeated a few times and no ratios greater than 10% were found. We take $\frac{\Delta \sigma_i^2}{\sigma_i^2}$ to be 10%, thereby the term in which it occurs contributes to a 15% fractional error in the retrieved dissipation rate. The fractional error in the horizontal wind is largely unknown. O'Connor et al. [2010] assume 1~2 m s^{-1} error and Shupe et al. [2012] assume a fractional error of 50%. We assume a fractional error of 15%, which is about 1 m s^{-1} out of the observed horizontal wind speed of 7 m s^{-1}. (A more conservative estimation of the uncertainty, say, 2 m s^{-1}, would not change the conclusion.) With Eq. (15) we conclude that a reasonable estimate of the fractional error in our retrieved dissipation rate is 30%.

Figure 6a shows the retrieved dissipation rates together with the profiles of the SGS dissipation rates at five time slices in the LOW and HIGH simulations. The SGS dissipation rates are smaller than the retrieved dissipation rates by nearly one order of magnitude. Because the turbulent broadening σ_t^2 is proportional to $\epsilon^{2/3}$, the turbulent broadening used in the forward model is only about 25% of that derived from the retrieved dissipation rates. (The solid and dashed red and blue lines without markers in Fig. 6b will be addressed later in Section 5.1.)

4.2. Shear broadening

As indicated by Eqs. (A2) and (A3), the shear broadening due to the horizontal and vertical shear of the vertical air velocity at a radar gate, σ_{sh}^2 and σ_{sv}^2, are proportional to the square of horizontal and vertical shear, k_h and k_v. In the recent literature, these two shear terms have been estimated from the difference of mean Doppler velocities observed in consecutive profiles or adjacent ranges [Shupe et al., 2008b; Fang et al., 2014; Borque et al., 2016]. For example, one can estimate the horizontal and vertical shear of the vertical air velocity as

$$k_h(z, t) = \frac{v_d(z, t + \Delta t) - v_d(z, t - \Delta t)}{2U\Delta t} \quad (16)$$

and

$$k_v(z, t) = \frac{v_d(z + \Delta z, t) - v_d(z - \Delta z, t)}{2\Delta z}. \quad (17)$$

By this definition, the horizontal shear broadening σ_{sh}^2 is proportional to $(v_d(z, t + \enspace t) - v_d(z, t - \enspace t))^2$. The ensemble mean of this squared velocity difference is exactly the definition of the second-order structure function of the velocity for a displacement of $2U \enspace t$ or $2 \enspace z$. This quantity is proportional to a weighted integral of the one-dimensional power spectra of the mean Doppler velocity. It has a significant contribution from the inertial subrange, which is turbulent in nature. In fact, the structure function calculated from the measured velocity time series can be used to retrieve the dissipation rate [e.g., Gultepe and Starr, 1995; Lothon et al., 2005]. The horizontal shear broadening calculated from the horizontal shear estimated with this approach overestimates the shear broadening by double-counting the contribution of the turbulent air motion associated with the inertial subrange. The calculation of vertical shear broadening not only suffers from the same problem but is also contaminated by the difference in the layer-mean of the reflectivity-weighted mean fall speed from one height to the next.

To minimize contamination of shear broadening estimates by turbulence and particle fall speeds, we estimated the horizontal and vertical shear of the vertical air velocity also following Eqs. (16) and (17) but with the mean Doppler velocity v_d in the equations replaced with a modified velocity. To be specific, we first filtered the mean Doppler velocity time series at each height with a one-dimensional Gaussian filter with a characteristic filter width equal to the integral length L used to retrieve the dissipation rates in Section 4.1. Then we removed the mean from the filtered series. Figure 7 exhibits the shear broadenings based on the observed and filtered mean Doppler velocity time series. The magnitude of the shear broadening is determined by both the magnitudes of the shear and the effective length over which the shear is applied (see Eqs A2 and A3). The vertical shear broadening shown in Fig. 7 has greater magnitude than the horizontal shear broadening because the vertical dimension of the radar sampling volume is greater than the horizontal dimension along the horizontal mean wind. In fact, the magnitudes of the vertical and horizontal shear are comparable (not shown). For the same reasons, the common practice of calculating the shear broadening in a forward model in the same way is also unreliable. We present this subsection as an intermediate step towards quantification of microphysical broadening in the observations and no comparison of shear broadening from the model and the observations is attempted.

4.3. Microphysical broadening

Microphysical broadening σ_{mp}^2 is obtained by removal of turbulence and shear broadening from the observed squared spectral width. Note that we ignore the beam width effect σ_{bw}^2 because with Eq. (A7) this term is estimated to be less than 2×10^{-4} m^2s^{-2} and much smaller than any other broadening terms. Figure 8 shows the observed squared spectral width for the liquid cloud layer and its decomposition into turbulent, shear, and microphysical broadening components for the layers where the dissipation rates are retrieved. The observed microphysical broadening is comparable with that from the HIGH simulation, while its lower bound is close to the microphysical broadening from the LOW simulation.

Note that the uncertainty of roughly 37–50% in the microphysical broadening σ_{mp}^2 decomposed from the observed squared spectral width corresponds to a 20% fractional error in the turbulent broadening, which is carried from the 30% fractional error in the retrieved dissipation rates. We assume no uncertainty in the layer-mean of the observed squared spectral width because the signal-noise-ratio of the MMCR observations from 17:00 UTC to 17:30 UTC is high (> 8 dB). The uncertainty in the shear broadening depends on the method to estimate it and very weakly on the uncertainty in the horizontal wind speed. We assume no uncertainty in the shear broadening.

5.   Discussion

With the quantification of the turbulent and shear broadening contributions to the observed squared spectral widths, we found that overly narrow modeled spectral widths are primarily caused by using the SGS dissipation rate to represent the dissipation rate in both the LOW and HIGH simulations and to a lesser degree contributed by the narrow microphysical broadening in the LOW simulation. In this section, we examine in more detail the two sources of the discrepancy in the Doppler spectral broadening terms.

5.1.   Turbulence in the simulations

We first investigate the underestimation of the retrieved dissipation rates calculated by DHARMA's SGS dissipation rates. A Smagorinsky SGS model builds on the assumption that the inertial subrange is partially captured in the simulated resolved flow. Ideally, one would expect that the power spectra of the resolved flow show a peak corresponding to large scale features, transit to a −5/3 slope corresponding to the inertial subrange behavior, then roll off at higher wavenumber range where the model is unable to resolve the kinetic energy. We examine the power spectra of the resolved vertical air velocity field to search for the expected behavior. Figure 9 shows the results in the lower and upper parts of the liquid cloud in the LOW and HIGH simulations at 4 h. The black dashed lines in the figures are the reference lines showing the expected inertial subrange power spectra assuming an isotropic three-dimensional Gaussian filter whose filter widths in three directions equal to that assumed in DHARMA formulation, that is, the standard deviations of the Gaussian pattern are

$$\sigma_1 = \sigma_2 = \sigma_3 = \frac{(\Delta x \Delta y \Delta z)^{1/3}}{\sqrt{12}},$$

where $x = y = 50$ m and $z = 15$ m are the grid spacings for LOW and HIGH simulations. Arguably there is a narrow wavenumber range showing a −5/3 slope in the power spectra in the lower part of the liquid cloud in both the LOW and HIGH simulations. Similar to the power spectra of the observed mean Doppler velocities, the power spectra of the simulated vertical wind fields in the upper part of the liquid cloud deviate from inertial subrange behavior. The power spectra were examined for the other four time slices from both the LOW and HIGH simulations and similar behavior was found.

If an inertial subrange is evident in the power spectra of the resolved flow, one could infer the dissipation rate from them. Ideally, the inferred dissipation rate should agree with those from the SGS model [Bou-Zeid et al., 2005; Pan and Chamecki, 2016]. Sullivan and Patton [2011] showed that, for a high resolution LES of a dry convective boundary layer, the velocity spectra demonstrated a continuous −5/3 slope from very close to the peak of the power to the highest resolved wavenumber, although only the underlying physics for the high wavenumber portion agreed with the inertial subrange. If the same behavior holds for our stratus-topped boundary layer, which is essentially a top-down convective boundary layer, we might be able to infer the dissipation rates in the DHARMA simulations from the power spectra that show evidence of an inertial subrange. The power spectra in Fig. 9a and Fig. 9b suggest dissipation rates greater than $10^{-3.5}$ m^{2}s^{-3}, approximately two times larger than those from the observations, and roughly a factor of 10 larger than those computed using the SGS eddy viscosity.

The large discrepancy between the inferred dissipation rates and those from the SGS model raises a question: what quantity shall we use in a forward model to represent the turbulence in the LES? Note that the power spectra in all panels in Fig. 9 fall off faster at high wavenumbers than the reference lines. This can be seen more clearly in Figs. 9e and 9f. which show the same power spectra as in Figs. 9a and 9b but flattened by multiplying with $\kappa_h^{5/3}$ to remove the wavenumber dependency. The reduced energy in the high wavenumber range is similar to that reported by Heinze et al. [2015], where the authors attributed this issue to the numerical limitations of the diffusion scheme as well as the errors associated with the time stepping scheme and/or spatial discretization.

It is known that an LES may suffer from both numerical errors and limitations in the SGS model [Chow and Moin, 2003]. The effects of numerical errors could be dissipative, that is, remove kinetic energy from the resolved flow. We diagnosed the numerical dissipation rate (D. Stevens, personal communication) and combined it with the SGS dissipation rate as an estimate of the total dissipation rate in the simulations. The profiles of the total dissipation rates are much closer to the retrieved dissipation rate profile (Fig. 6b) and more comparable to the dissipation rates inferred from the power spectra of DHARMA's resolved flow. The agreement between the total dissipation rate (D) and the difference (D') between the TKE tendency and its individual budget terms, i.e., buoyancy, shear, and transport, in Fig. 10 also suggests that the total dissipation rate better represents the TKE dissipation rate in the DHARMA simulation evaluated here than the SGS dissipation rate.

Ideally, the impacts of numerical error on the solution to an LES' governing equations are smaller than the terms parameterized with a physically based SGS model. However, this is not always the case. The impacts of numerical error depend on not only the specifics of the numerical scheme but also on the grid spacing to the filter width ratio [Ghosal 1996; Meyers et al., 2007], the choice of which depends on the characteristics of the flow and is limited by computational cost considerations. In the simulations we evaluated here, the total (i.e., combined SGS and numerical) dissipation rate is about six times the SGS dissipation rate within the liquid cloud layer. In contrast to this study, Rémillard et al. [2017] found that the turbulent broadening from the MMCR observations agreed well with that modeled based on

the SGS dissipation rates reported by DHARMA and another LES model simulating a marine stratocumulus case, thus arousing no suspicions. Our diagnosis using DHARMA output from that case study (not shown) indicates that the total dissipation rate was about three times the SGS dissipation rate and that the dissipation rate inferred from the power spectra of the resolved vertical velocity was much closer to the SGS dissipation rate than in the case reported here. Thus, the SGS dissipation rate in DHARMA appears to represent a variable fraction of the true total rate that is quite strongly case-dependent.

Our evaluation results also warrant future tests of more advanced SGS models, for example, the dynamic mixed SGS model by Zang et al. [1993], which have been incorporated in DHARMA but not been evaluated here. These SGS models explicitly include the modified Leonard component of the SGS stress tensor and aim to reconstruct the stresses that are damped due to the presence of a filter that is not sharp in spectral space and hence more accurately represent the turbulence dissipation.

Although numerical dissipation dominates energy dissipation in the simulations evaluated here, some inertial subrange behavior is seen in the power spectra of the resolved flow, and the dissipation rate inferred from the power spectra agrees with those from the observations as well as the total dissipation rates in the model. We conclude that the best practice for estimating representative dissipation rates in an LES, needed for radar Doppler spectra forward modeling, is to infer this rate from the power spectra of the resolved flow or from the sum of the SGS dissipation rate and numerical dissipation rate. We note that both methods pose a setback for forward modeling studies insofar as power spectra and estimates of numerical dissipation offer only domain-mean profiles rather than grid cell values of the dissipation rate as used in Rémillard et al. [2017]. This is likely to present a limitation especially to use of forward simulation of Doppler spectra within horizontally heterogeneous cloud fields such as cumulus.

5.2. Ice particle fall speeds

Microphysical broadening represents the variance of the particle reflectivity versus particle fall speed distribution. We interpret the retrieved and modeled microphysical broadening together with the reflectivity-weighted mean fall speed. The layer-mean of reflectivity-weighted mean fall speed can be estimated by taking the layer-mean of the mean Doppler velocity with the assumption that the layer-mean of the vertical air velocity is zero [Orr and Kropfli, 1999]. Combining the results presented earlier in Fig. 3b and Fig. 8, for both the reflectivity-weighted mean fall speed and layer-mean microphysical broadening, the HIGH simulation agrees better with the observations than the LOW simulation, suggesting that ice particles in the HIGH simulation have a wider spread in fall speed and fall faster on average. Note that we reproduced the results in Avramov et al. [2011] that both simulations very well reproduce the distribution of mean Doppler velocities (indicating realistic vertical wind speeds), but the HIGH simulation could not reproduce the high reflectivities observed by the MMCR. All results from evaluations against the MMCR observations, combined with the previous finding by Avramov et al. [2011] that the HIGH simulation could not reproduce the concentrations of the largest particles observed in situ, provide a more thorough picture of different strengths and limitations of the LOW and HIGH simulations. When all ice particles

are assumed to be at the high-density limit (in HIGH), fast falling ice particles are produced. However, the largest ice particles are too heavy to remain lofted; their substantially faster fall speed resulted in relatively too few large ice particles (despite comparable numbers of mid-sized ice particles) and an associated deficit of reflectivity compared with observations. In contrast, the slower falling ice particles in the LOW simulation experienced longer growth periods in the liquid cloud layer and reached larger sizes at higher concentrations, resulting in higher reflectivities. However, these large ice particles fall at similar speeds, resulting in narrower microphysical broadening. In fact, with the calculated fall speed from low-density aggregate properties reaching a maximum value at ~0.5 m s^{-1} (Fig. 2a), we note that it is not possible for the LOW simulation to produce a reflectivity-weighted mean fall speed exceeding 0.5 m s^{-1} as was observed in the lower parts of the sub-cloud layer (Fig. 3b).

As noted above, Avramov et al. [2011] selected the LOW and HIGH ice properties to bound the range of dendrites observed. When taken together with uncertainty in retrieved microphysical broadening, our results suggest that the actual mixture of ice particle densities may be important to microphysical spectral broadening. It may be the case, for instance, that spectral broadening is significantly increased by contributions of high-density ice particles whereas reflectivity and concentrations of the largest particles are significantly increased by the contributions of low-density ice particles. A high-fidelity reproduction of the observed ice particle population requires the correct representation of not only the fall speeds but also many other processes, including but not limited to the dynamics as well as the ice nucleation processes, which are challenging tasks to accomplish in a physically consistent and rigorous manner in models, especially in the absence of quantitative ice property information from measurements [e.g., Fridlind et al., 2012]. Our method of retrieving microphysical broadening provides an additional means to assess simulation veracity by using the additional information provided by radar Doppler spectra.

This method is inevitably affected by the assumptions in the calculation of ice particle scattering properties. Ice mass in our specific case is dominated by big dendrites and aggregates. Assuming these ice particles fall with their maximum dimension close to the horizontal plane, Botta et al. [2011] showed that the reflectivities of the ice particles are close to the results assuming Rayleigh scattering when viewed from below while resonance effects are more evident in the reflectivity at side incidence. We expect small uncertainty due to ice particle scattering properties for our case. For more complicated cases, the sensitivity of the results to the scattering calculations may need to be explored.

6. Summary and Conclusions

In this work, we extended previous evaluation of DHARMA simulations of a single-layer, mixed-phase cloud observed on April 8, 2008, at the NSA site. Two sets of simulations were evaluated, one assuming low density ice particles (LOW) and the other one assuming high density ice particles (HIGH), intended to bound the range of dendrite types observed. The goal was to extend the previous evaluation to compare Doppler spectral widths with those observed by the MMCR. We retrieved the dissipation rates from the MMCR observations, decomposed the observed spectral widths into their turbulent, shear, and microphysical

broadening terms, and then compared them with broadening terms calculated for the simulations with a forward model.

To accurately retrieve dissipation rates as well as each broadening term from the observations, a few modifications to previously presented techniques were made. First, we showed that the inertial subrange spectra filtered with the radar sampling volume is a better underlying model than the unfiltered −5/3 law for the retrieval of the dissipation rate from the power spectra of the mean Doppler velocity. Second, we demonstrated that filtering out turbulence and removal of the layer-mean reflectivity-weighted mean fall speed from the observed mean Doppler velocity is important in avoiding overestimation of the shear broadening. We also provided a method to quantify the uncertainty in the retrieved dissipation rates, which eventually propagates to the uncertainty in the microphysical broadening.

The turbulent broadening σ_t^2 (with a layer-mean around 0.033 m^2 s^{-2} in the lower part of the liquid cloud, corresponding to a width of 0.18 m s^{-1}) accounts for roughly 62–69% of the observed squared spectral widths (around 0.051 m^2 s^{-2} or 0.22 m s^{-1}) in our case. It is underestimated by both the LOW and HIGH simulations because the LES SGS dissipation rates severely underestimate the observed in-cloud dissipation rate in this case by nearly a factor of 10. The domain-mean profile of the total dissipation rates, estimated as the SGS dissipation rates plus the numerical dissipation rates, are much closer to the dissipation rates retrieved from the observations. We examined power spectra of the simulated vertical air velocity and found a short inertial subrange in both simulations. The dissipation rates inferred from the power spectra of the simulated vertical air velocity are comparable to those from the observations and the total dissipation rates (within a factor of two). The dominance of the numerical dissipation rates over the SGS dissipation rates in the simulations are also consistent with the reduced energy in the high wavenumber range in the model. We show that the power spectra of the simulated velocity field can be examined in this stratiform cloud case to check the performance of the SGS model in the LES if the numerical dissipation rates are not readily diagnosed.

The microphysical broadening σ_{mp}^2 (with a layer-mean around 0.016 m^2 s^{-2} in the lower part of the liquid cloud, corresponding to a width of 0.13 m s^{-1}) contributes 28–34% of the observed squared spectral width in this case study, whereas turbulent broadening contributes the majority of the remainder. The HIGH simulation produced microphysical broadening comparable with that retrieved from the observations, whereas the LOW simulation underestimated the microphysical broadening by an amount greater than the retrieval uncertainty of 37–50% (based on σ_{mp}^2, or 17–29% based on σ_{mp}). The HIGH simulation also better matchedhorizontally averaged mean Doppler velocity. However, Avramov et al. [2011] demonstrated that the faster-falling aggregates in the HIGH simulation are not maintained at high enough concentrations compared with radar and in situ observations. We therefore posit that a mixture of particle types or possible uncertainty in ice particle properties (which are not obtained from observations in a quantitative manner), their fall speeds (calculated from the properties), or ice nucleation could be additionally required in order to achieve agreement with multiple observational measures. Some of these sources of

uncertainty have been emphasized in past studies [e.g., Fridlind et al., 2012]. Our results show that a comparison between simulated and observed microphysical broadening can provide another such useful evaluative measure of the ice properties in high-resolution simulations.

Acknowledgments

Appendix.: Forward Model

We constructed a forward model adapted from the framework in Kollias et al. [2011a] according to the following few steps. First, a "quiet-air" spectrum is calculated for each model grid box by weighting the fall speed by the total hydrometeor backscattering cross section for all hydrometeor types/sizes associated with each bin of the particle size distribution, in this case including liquid cloud droplets, pristine ice, and aggregates. This "quiet-air" spectrum is only broadened by microphysical factors, i.e., hydrometeor fall speeds and backscattering cross sections. Then we calculated the turbulent broadening σ_t^2, shear broadening σ_s^2, and the beamwidth effect σ_{bw}^2. Then, the "quiet-air" spectrum is shifted by the resolved vertical air velocity, that is, the simulated w-wind, and convolved with a normal distribution following

$$N\left(0, \sigma_{dyn}^2 = \sigma_t^2 + \sigma_s^2 + \sigma_{bw}^2\right). \quad \text{(A1)}$$

One spectrum is constructed for one model grid box containing hydrometeors. Finally, noise with characteristics consistent with the MMCR is added following Zrnić [1975]. The resulting spectrum is then processed in the same way as an observed spectrum. First, the noise floor is identified following Hildebrand and Sekhon [1974]. And second, spectra containing fewer than four consecutive (positive value) spectral points after the removal of the noise floor are discarded.

The turbulent broadening σ_t^2 is computed following Eq. (10). To be consistent withcommon practice, the dissipation rates from the DHARMA SGS model are used to calculate $\Phi_{33}(\boldsymbol{\kappa})$ following Eq. (4). Parameters required for the calculation of $\left|\hat{G}(\boldsymbol{\kappa})\right|^2$ following Eq. (11) are consistent with configurations of the MMCR together with a constant horizontal wind speed of 7.1 m s^{-1} based on the nearly uniform horizontal wind speed measured by aradiosonde throughout the liquid cloud layer. The limits of the integral are set to wavelengths from 1000 m to 1 mm, which may overestimate the turbulent broadening if the actual outer length scale

of the inertia subrange is shorter than 1000 m. The overestimation is up to 10% as long as the inertial subrange extends to scales greater than around 125 m.

The calculation of the shear broadening σ_s^2 is similar to Eqs (5.74) ~ (5.76) in Doviak and Zrni [1993] but takes into account the impacts of the horizontal wind speed on the beam dimension. To be specific, the shear broadening is the sum of two terms, i.e., the broadening by the horizontal and vertical shear of the vertical air velocity:

$$\sigma_{sh}^2 = \left(\frac{z^2\theta^2}{16\log(2)} + \frac{U^2(z)T^2}{12} \right) k_h^2, \quad \text{(A2)}$$

and

$$\sigma_{sv}^2 = (0.35c\tau)^2 k_v^2. \quad \text{(A3)}$$

In these equations, the horizontal and vertical shear of the vertical air velocity is calculated from the model resolved vertical air velocity field. For example, for a grid box at (x, y, z),

$$k_h^2 = \left(\frac{w(x + \Delta x, y, z) - w(x - \Delta x, y, z)}{2\Delta x} \right)^2 + \left(\frac{w(x, y + \Delta y, z) - w(x, y - \Delta y, z)}{2\Delta y} \right)^2, \quad \text{(A4)}$$

and

$$k_v^2 = \left(\frac{w(x, y, z + \Delta z) - w(x, y, z - \Delta z)}{2\Delta z} \right)^2, \quad \text{(A5)}$$

where $x =$ $y = 50$ m and $z = 15$ m are the grid spacings for LOW and HIGH simulations.

The beamwidth effect is calculated as

$$\sigma_{bw}^2 = \frac{U^2(z)\theta^2}{16\log(2)}. \quad \text{(A6)}$$

References

Ackerman AS, Toon OB, and Hobbs PV (1995), A model for particle microphysics, turbulent mixing, and radiative-transfer in the stratocumulus-topped marine boundary layer and comparisons with measurements, J. Atmos. Sci, 52(8), 1204–1236, doi: 10.1175/1520-0469 (1995)052<1204:AMFPMT>2.0.CO;2.

Ackerman AS, Kirkpatrick MP, Stevens DE, and Toon OB (2004), The impact of humidity above stratiform clouds on indirect aerosol climate forcing, Nature, 432 (7020), 1014–1017, doi: 10.1038/ nature03174. [PubMed: 15616559]

Avramov AE, Ackerman AS, Fridlind AM, van Diedenhoven B, Botta G, Aydin K, Verlinde J, Korolev A, Strapp W, McFarquhar GM, Jackson R, Brooks SD, Glenn A, and Wolde M (2011), Towards ice formation closure in Arctic mixed-phase boundary layer clouds during ISDAC, J. Geophys. Res, 116, D00T08, doi: 10.1029/2011JD015910.

Borque P, Luke E, and Kollias P (2016), On the unified estimation of turbulence eddy dissipation rate using Doppler cloud radars and lidars, J. Geophys. Res, 120, doi: 10.1002/2015JD024543.

Botta G, Aydin K, Verlinde J, Avramov AE, Ackerman AS, Fridlind AM, McFarquhar GM, and Wolde M (2011), Millimeter wave scattering from ice crystals and their aggregates: Comparing cloud model simulations with X- and Ka-band radar measurements, J. Geophys. Res, 116, D00T04, doi: 10.1029/2011JD015909.

Bou-Zeid E, Meneveau C, and Parlange M (2005), A scale-dependent Lagrangian dynamic model for large eddy simulation of complex turbulent flows, Phys. Fluids, 17(2), 025105.

Chow FK, and Moin P (2003), A further study of numerical errors in large-eddy simulations, J. Comput. Phys, 184(2), 366–380.

Curry JA, Schramm JL, Rossow WB, and Randall D (1996), Overview of Arctic cloud and radiation characteristics, J. Climate, 9 (8), 1731–1764.

Deng M, and Mace GG (2006), Cirrus microphysical properties and air motion statistics using cloud radar Doppler moments. Part I: Algorithm description, J. Appl. Meteorol. Clim, 45 (12), 1690–1709.

Dias NL (2017), Smoothed spectra, ogives, and error estimates for atmospheric turbulence data, Bound.-Lay. Meteorol, doi: 10.1007/s10546-017-0293-7.

Doviak RJ, and Zrni D (1993), Doppler Radar and Weather Observations, 562 pp., Academic Press.

Fang M, and Doviak RJ (2008), Coupled contributions in the Doppler radar spectrum width equation, J. Atmos. Ocean. Technol, 25 (12), 2245–2258.

Fang M, Doviak RJ, and Albrecht BA (2011), Significance of the coupled term in the Doppler weather radar spectrum width equation, J. Atmos. Ocean. Technol, 28(4), 539–547.

Fang M, Albrecht BA, Ghate VP, and Kollias P (2014), Turbulence in continental stratocumulus, Part II: Eddy dissipation rates and large-eddy coherent structures, Bound.-Lay. Meteorol, 150(3), 361–380.

Fridlind AM, Ackerman AS, McFarquhar G, Zhang G, Poellot MR, DeMott PJ, Prenni AJ, and Heymsfield AJ (2007), Ice properties of single-layer stratocumulus during the Mixed–Phase Arctic Cloud Experiment: 2. Model results, J. Geophys. Res, 112, D24202, doi: 10.1029/2007JD008646.

Fridlind AM, van Diedenhoven B, Ackerman AS, Avramov A, Mrowiec A, Morrison H, Zuidema P, and Shupe MD (2012), A FIRE-ACE/SHEBA case study of mixed-phase Arctic boundary-layer clouds: Entrainment rate limitations on rapid primary ice nucleation processes, J. Atmos. Sci, 69, 365–389, doi: 10.1175/JAS-D-11-052.1.

Ghosal S (1996), An analysis of numerical errors in large-eddy simulations of turbulence, J. Comput. Phys, 125(1), 187–206.

Gultepe I, and Starr DO (1995), Dynamical structure and turbulence in cirrus clouds: Aircraft observations during fire, J. Atmos. Sci, 52 (23), 4159–4182.

Intrieri JM, Shupe MD, Uttal T, and McCarty BJ (2002), An annual cycle of Arctic cloud characteristics observed by radar and lidar at SHEBA, J. Geophys. Res, 107 (C10), 8030, doi: 10.1029/2000JC000423.

Heinze R, Mironov D, and Raasch S (2015), Second-moment budgets in cloud topped boundary layers: A large-eddy simulation study, J. Adv. Model. Earth Sy, 7, 510–536, doi: 10.1002/2014MS000376.

Hildebrand PH, and Sekhon RS (1974), Objective determination of the noise level in Doppler spectra, J. Appl. Meteorol, 13(7), 808–811.

Kaimal JC, and Finnigan JJ, Atmospheric Boundary Layer Flows: Their Structure and Measurement, 289 pp., Oxford Univ. Press, New York, 1994.

Kay JE, L'Ecuyer T, Gettelman A, Stephens G, and O'Dell C (2008), The contribution of cloud and radiation anomalies to the 2007 Arctic sea ice extent minimum, Geophys. Res. Lett, 35(8).

Kirkpatrick MP, Ackerman AS, Stevens DE, and Mansour NN (2006), On the application of the dynamic Smagorinsky model to large-eddy simulations of the cloud-topped atmospheric boundary layer, J. Atmos. Sci, 63(2), 526–546.

Kollias P, Miller MA, Luke EP, Johnson KL, Clothiaux EE, Moran KP, Widener KB, and Albrecht BA (2007), The atmospheric radiation measurement program cloud profiling radars: Second-generation sampling strategies, processing, and cloud data products, J. Atmos. Ocean. Technol, 24(7), 1199–1214.

Kollias P, Rémillard J, Luke E, and Szyrmer W (2011a), Cloud radar Doppler spectra in drizzling stratiform clouds: 1. forward modeling and remote sensing applications, J. Geophys. Res, 116 (D13), D13201.

Kollias P, Szyrmer W, Rémillard J, and Luke E (2011b), Cloud radar Doppler spectra in drizzling stratiform clouds: 2. observations and microphysical modeling of drizzle evolution, J. Geophys. Res.-Atmos, 116 (D13).

Lothon M, Lenschow DH, Leon D, and Vali G (2005), Turbulence measurements in marine stratocumulus with airborne Doppler radar, Q. J. Roy. Meteor. Soc, 131 (609), 2063–2080.

Maahn M, and Lohnert U (2017), Potential of higher-order moments and slopes of the radar Doppler spectrum for retrieving microphysical and kinematic properties of Arctic ice clouds, J. Appl. Meteorol. Clim, 56(2), 263–282.

Maahn M, Lohnert U, Kollias P, Jackson RC, and McFarquhar GM (2015), Developing and evaluating ice cloud parameterizations for forward modeling of radar moments using in situ aircraft observations, J. Atmos. Ocean. Technol, 32(5), 880–903.

McFarquhar GM, Ghan S, Verlinde J, Korolev A, Strapp JW, Schmid B, Tomlinson JM, Wolde M, Brooks SD, Cziczo D, Dubey MK, Fan J, Flynn C, Gultepe I, Hubbe J, Gilles MK, Laskin A, Lawson P, Leaitch WR, Liu P, Liu X, Lubin D, Mazzoleni C, Macdonald AM, Moffet RC, Morrison H, Ovchinnikov M, Shupe MD, Turner DD, Xie S, Zelenyuk A, Bae K, Freer M, and Glenn A (2011), Indirect and Semi-Direct Aerosol Campaign (ISDAC): The impact of Arctic aerosols on clouds, Bull. Amer. Meteor. Soc, 92, 183–201, doi: 10.1175/2010BAMS2935.1.

Meyers J, Geurts BJ, and Sagaut P (2007), A computational error-assessment of central finite-volume discretizations in large-eddy simulation using a Smagorinsky model, J. Comput. Phys, 227(1), 156–173.

O'Connor EJ, Illingworth AJ, Brooks IM, Westbrook CD, Hogan RJ, Davies F, and Brooks BJ (2010), A method for estimating the turbulent kinetic energy dissipation rate from a vertically-pointing Doppler lidar, and independent evaluation from balloon-borne in-situ measurements, J. Atmos. Ocean. Technol, 27, 1652–1664.

Orr BW, and Kropfli RA (1999), A method for estimating particle fall velocities from vertically pointing Doppler radar. J. Atmos. Ocean. Technol, 16, 29–37.

Pan Y, and Chamecki M (2016), A scaling law for the shear-production range of second-order structure functions, J. Fluid Mech, 801, 459–474.

Persson POG, Shupe MD, Perovich D, and Solomon A (2017), Linking atmospheric synoptic transport, cloud phase, surface energy fluxes, and sea-ice growth: observations of midwinter SHEBA conditions, Clim. Dynam, 49(4), 1341–1364.

Pope SB (2000), Turbulent Flows, 809 pp., Cambridge University Press.

Rambukkange MP, Verlinde J, Eloranta EW, Flynn CJ, and Clothiaux EE (2011), Using Doppler spectra to separate hydrometeor populations and analyze ice precipitation in multilayered mixed-phase clouds, IEEE Geosci. and Remote S, 8(1), 108–112, doi: 10.1109/LGRS.2010.2052781.

Rémillard J, Fridlind AM, Ackerman AS, Tselioudis G, Kollias P, Mechem DB, Chandler HE, Luke E, Wood R, Witte MK, Chuang PY, and Ayers JK (2017), Use of cloud radar Doppler spectra to evaluate stratocumulus drizzle size distributions in large-eddy simulations with size-resolved microphysics, J. Appl. Meteorol. Clim, 56 (12), 3263–3283.

Sedlar J, Tjernström M, Mauritsen T, Shupe MD, Brooks IM, Persson POG, Birch CE, Leck C, Sirevaag A, and Nicolaus M (2011), A transitioning Arctic surface energy budget: the impacts of solar zenith angle, surface albedo and cloud radiative forcing, Clim. Dynam, 37 (7–8), 1643–1660.

Shupe M, Matrosov S, and Uttal T (2006), Arctic mixed-phase cloud properties derived from surface-based sensors at SHEBA, J. Atmos. Sci, 63, 697–711.

Shupe MD, Daniel JS, De Boer G, Eloranta EW, Kollias P, Luke EP, Long CN, Turner DD, and Verlinde J (2008a), A focus on mixed-phase clouds: The status of ground-based observational methods, Bull. Amer. Meteor. Soc, 89 (10), 1549–1562.

Shupe MD, Kollias P, Poellot M, and Eloranta E (2008b), On deriving vertical air motions from cloud radar Doppler spectra, J. Atmos. Ocean. Technol, 25(4), 547–557.

Shupe MD, Walden VP, Eloranta E, Uttal T, Campbell JR, Starkweather SM, and Shiobara M (2011), Clouds at Arctic atmospheric observatories. Part I: Occurrence and macrophysical properties, J. Appl. Meteorol. Clim, 50 (3), 626–644.

Shupe M, Brooks I, and Canut G (2012), Evaluation of turbulent dissipation rate retrievals from Doppler cloud radar, Atmos. Meas. Tech, 5(6), 1375–1385.

Stevens DE, Ackerman AS, and Bretherton CS (2002), Effects of domain size and numerical resolution on the simulation of shallow cumulus convection, J. Atmos. Sci, 59 (23), 3285–3301, doi: 10.1175/1520-0469 (2002)059<3285:EODSAN>2.0.CO;2.

Sullivan PP, and Patton EG (2011), The effect of mesh resolution on convective boundary layer statistics and structures generated by large-eddy simulation, J. Atmos. Sci, 68 (10), 2395–2415.

Toon OB, McKay CP, Ackerman TP, and Santhanam K (1989), Rapid calculation of radiative heating rates and photodissociation rates in inhomogeneous multiple scattering atmospheres, J. Geophys. Res, 94 (D13), 16,287–16,301, doi: 10.1029/JD094iD13p16287.

Turner DD, Clough SA, Liljegren JC, Clothiaux EE, Cady-Pereira KE, and Gaustad KL (2007), Retrieving liquid water path and precipitable water vapor from the Atmospheric Radiation Measurement (ARM) microwave radiometers, IEEE T. Geosci. Remote, 45 (11), 3680–3690.

White AB, Lataitis RJ, and Lawrence RS (1999), Space and time filtering of remotely sensed velocity turbulence, J. Atmos. Ocean. Technol, 16, 1967–1972.

Zang Y, Street RL, and Koseff JR (1993), A dynamic mixed subgrid-scale model and its application to turbulent recirculating flows, Phys. Fluids A-Fluid, 5 (12), 3186–3196.

Zrni DS (1975), Simulation of weatherlike Doppler spectra and signals, J. Appl. Meteorol, 14, 619–620.

Key Points:

- Model subgrid-scale dissipation rates should be used with caution in characterizing turbulence in forward modeling of radar Doppler spectra.

- Microphysical broadening retrieved from observations of Arctic mixed-phase clouds provides additional measures for model evaluation.

- Quantification of turbulent and shear broadening and their uncertainties are critical for accurate retrieval of the microphysical broadening.
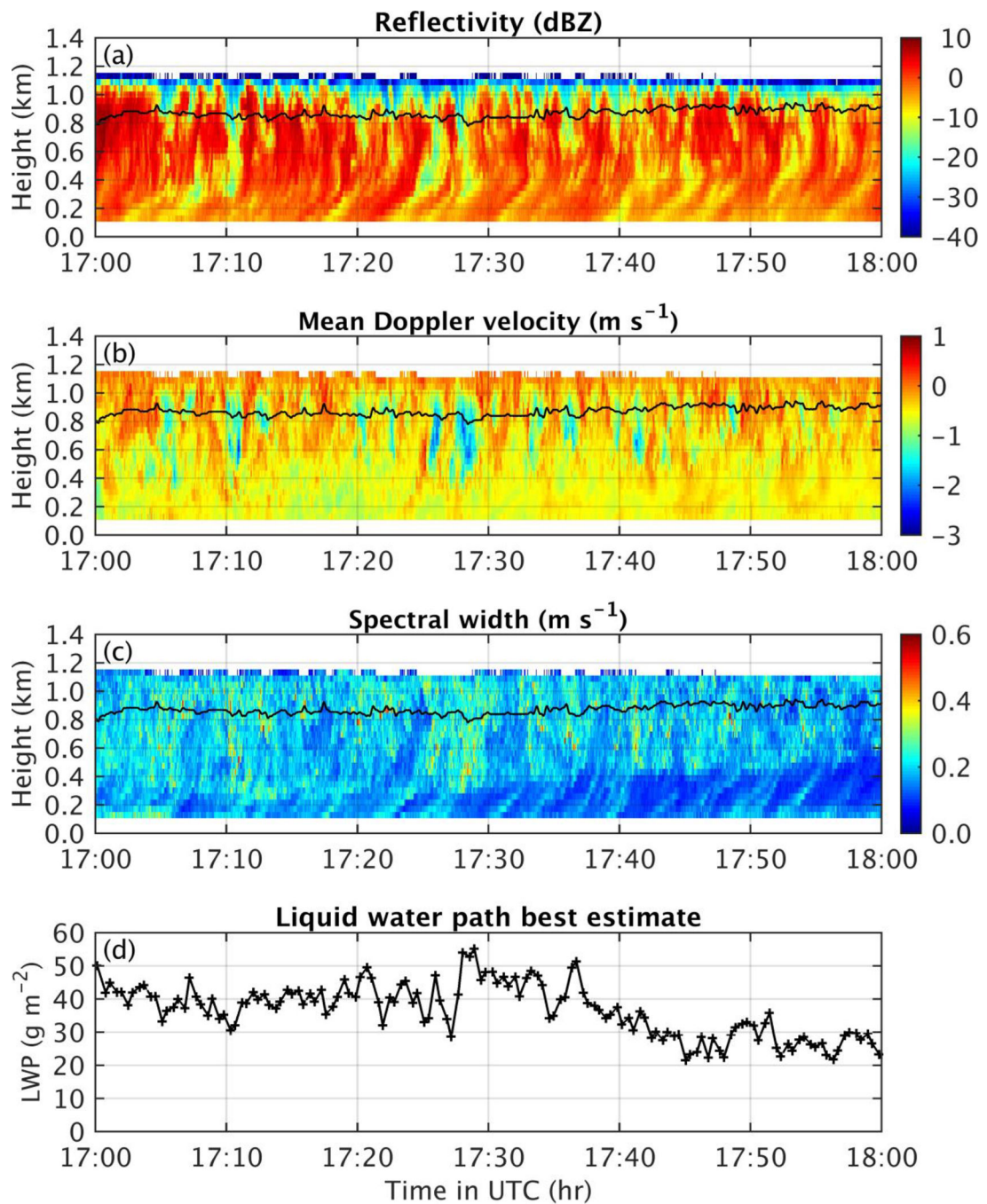
Figure 1.
(a) Reflectivity, (b) mean Doppler velocity (with positive values indicating upward motion), and (c) Doppler spectral width measured by the MMCR at the DOE ARM CRF on the NSA from 17:00 UTC to 18:00 UTC, April 8, 2008. The black solid line in each panel is the cloud base height from a ceilometer. Panel (d) shows the time series of liquid water path retrieved from a microwave radiometer.
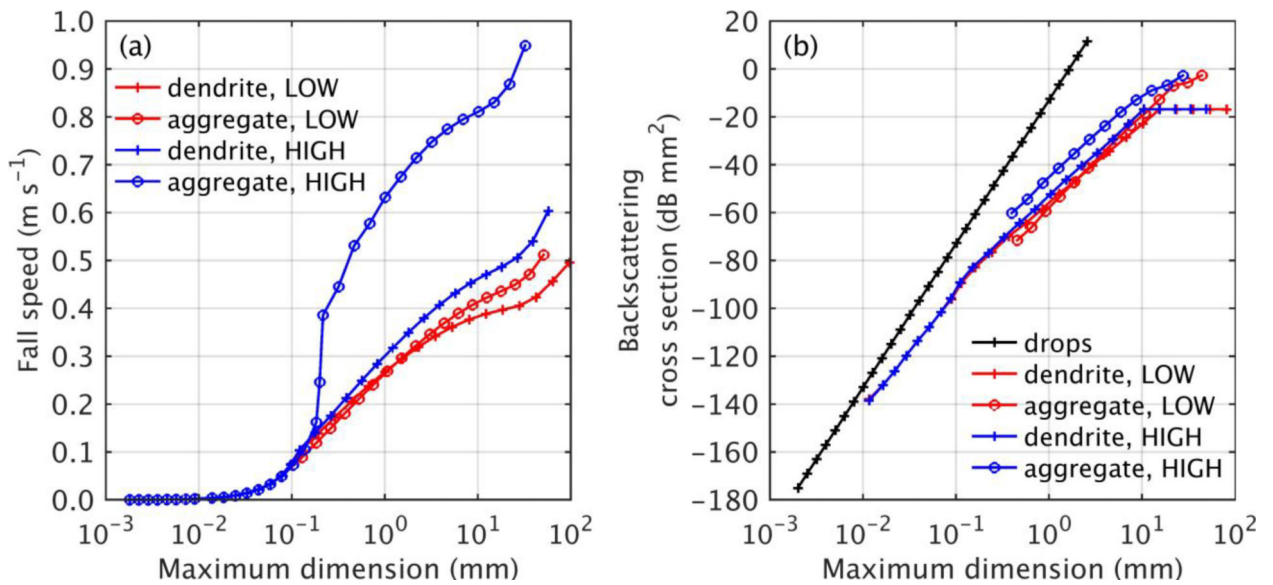
Figure 2.
(a) Fall speed versus the maximum dimension of ice particle used in the low density ice particle simulation (LOW) and the high density ice particle simulation (HIGH). (b) Backscattering cross sections of the hydrometeor particles in the Ka-band versus their maximum dimension, which is identical to the diameter for spherical particles. The backscattering cross sections of liquid drops are calculated with Rayleigh scattering. The backscattering cross sections of ice particles are calculated with the Generalized Multi-particle Mie (GMM) method.
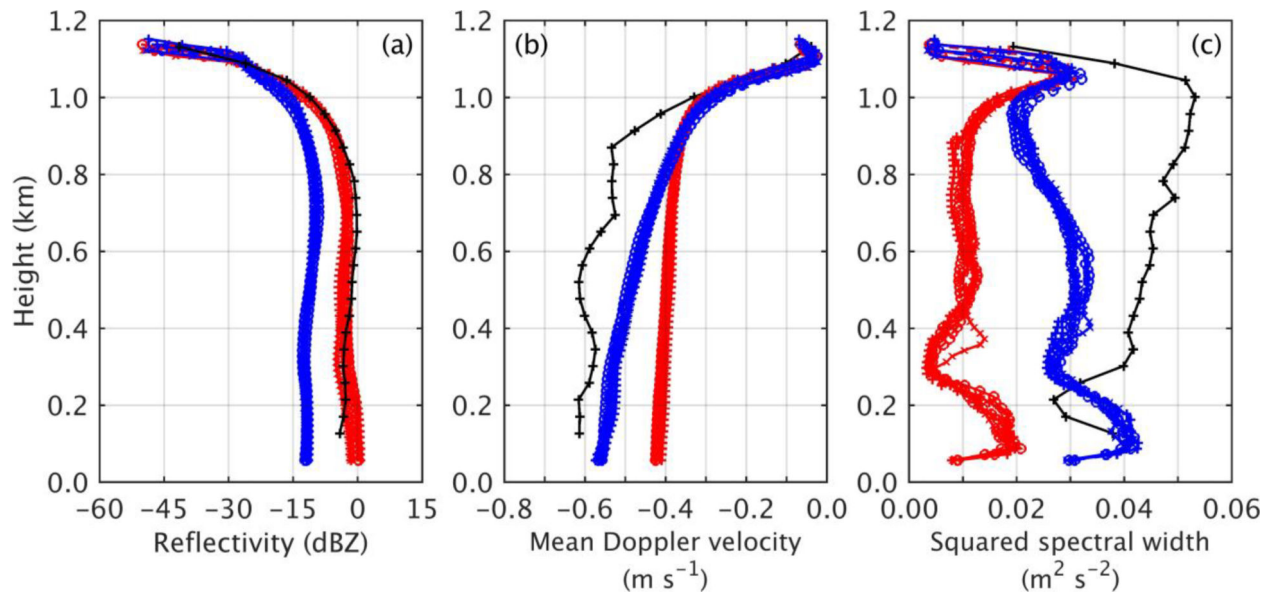
Figure 3.
Observed and modeled layer-mean values of (a) reflectivities, (b) the mean Doppler velocities, and (c) squared spectral widths. The red lines represent the modeled layer-means of the mean Doppler velocities for five time slices of the LOW simulation, whereas the blue lines represent these same layer-means for five time slices of the HIGH simulation. Profiles for DHARMA simulations are shifted up for 50 m to compensate for the different location of liquid cloud in simulations and observation.
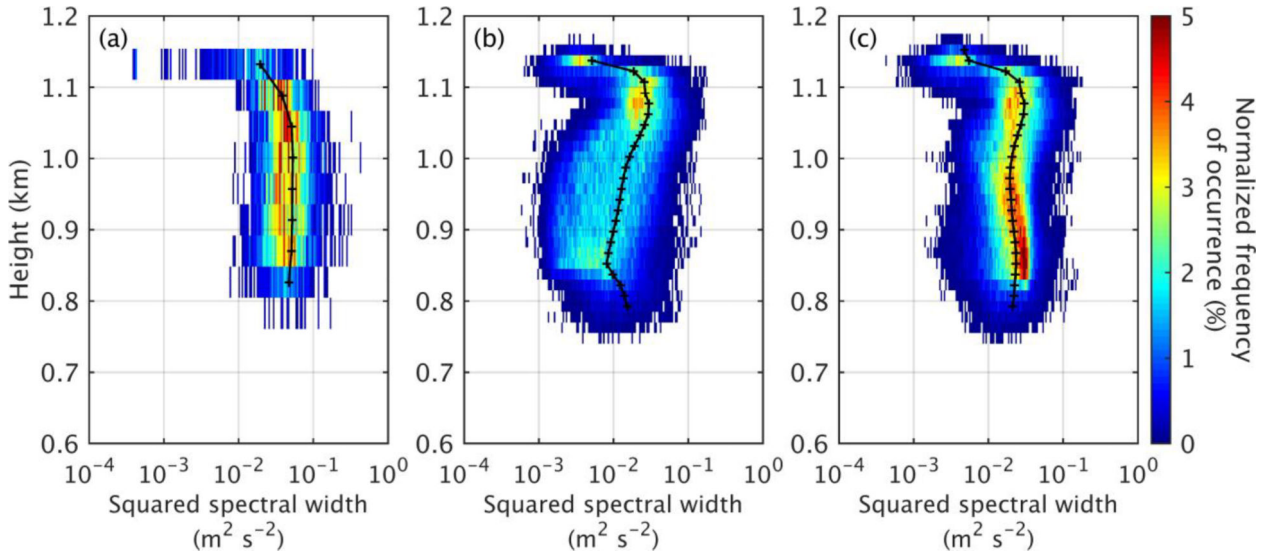
Figure 4.
Normalized frequency of occurrence of squared Doppler spectral widths by height for (a) the
observations, (b) the LOW simulation at 4 h, and (c) the HIGH simulation at 4 h. The
frequency of occurrence is binned every 0.02 decade and normalized (for the observations)
by the total number of profiles from 17:00 UTC to 17:30 UTC, April 8, 2008, and (for the
simulations) by the total number of grid points at each model layer. The black solid line with
crosses in each panel shows the root mean squared spectral widths with height.
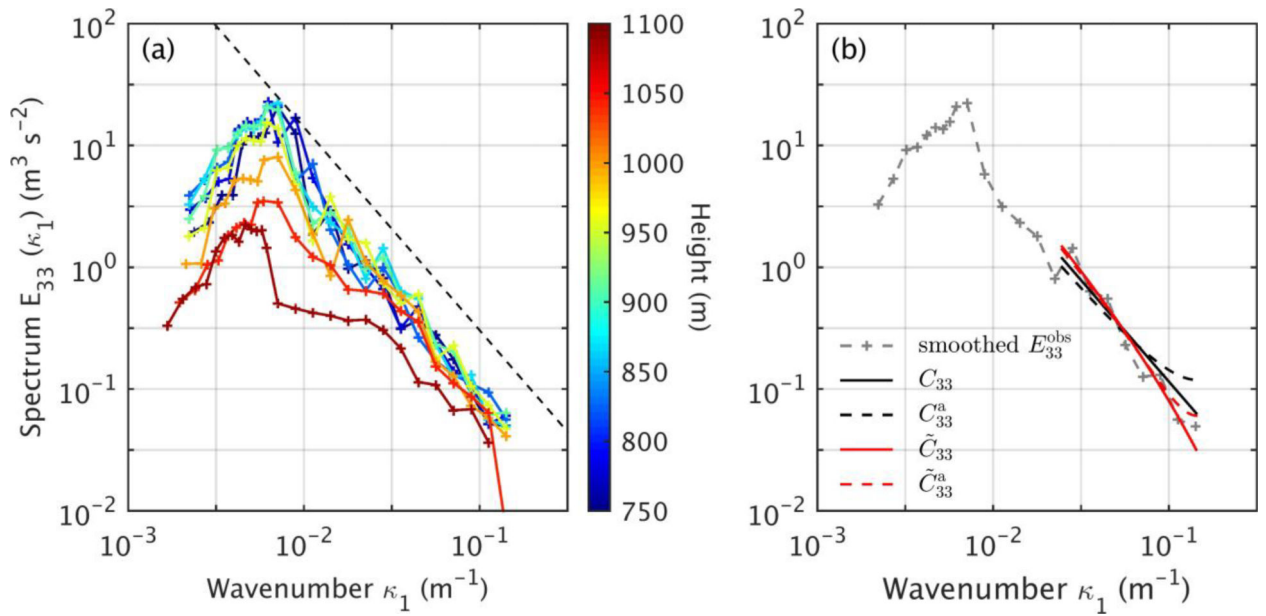
Figure 5.
(a) Power spectra of the detrended observed mean Doppler velocities. Colors of lines indicate the heights of the radar sampling volumes. Spectra for scales shorter than 1000 m (wavenumber of $10^{-2.2}$ m^{-1}) are smoothed by averaging over non-overlapping wavenumber ranges of 0.1 decade. Spectra for scales longer than 1000 m are smoothed by 8-point moving average. Black dashed line is a reference line showing −5/3 slope. (b) Power spectra based on four underlying models and corresponding retrieved dissipation rates at 870.2 m. Gray smoothed spectrum is the same as the one in (a) for the same height.
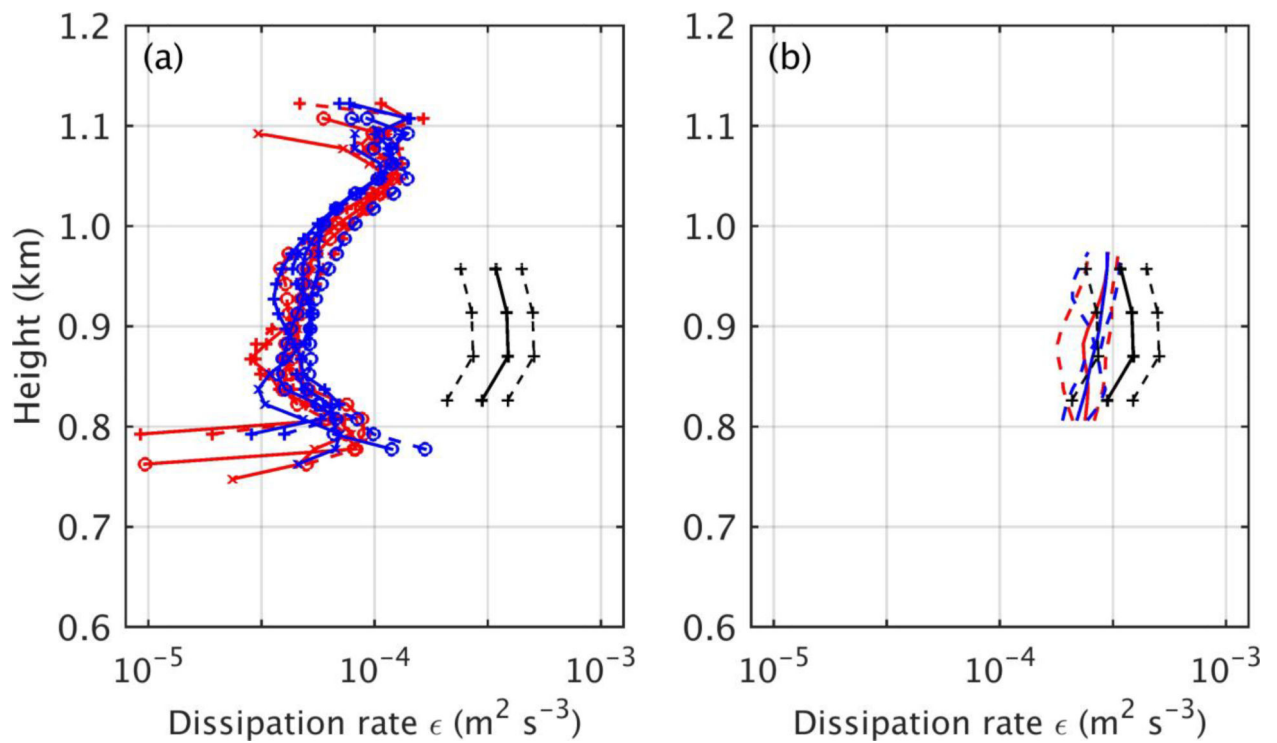
Figure 6.
Comparison of the dissipation rates retrieved from the observations (black solid line), along with their uncertainties (black dashed lines), based on assuming filtered inertial subrange spectra without aliasing to (a) those from the subgrid-scale (SGS) model for the five time slices from the LOW (red lines with markers) and HIGH (blue lines with markers) simulations and to (b) the mean (solid lines), as well as minimum and maximum (dashed lines), total dissipation rates from the LOW (red lines) and HIGH (blue lines) simulations. Profiles for the DHARMA simulations are shifted up in height by 50 m to compensate for the difference in location of the liquid cloud in the simulations and observations.
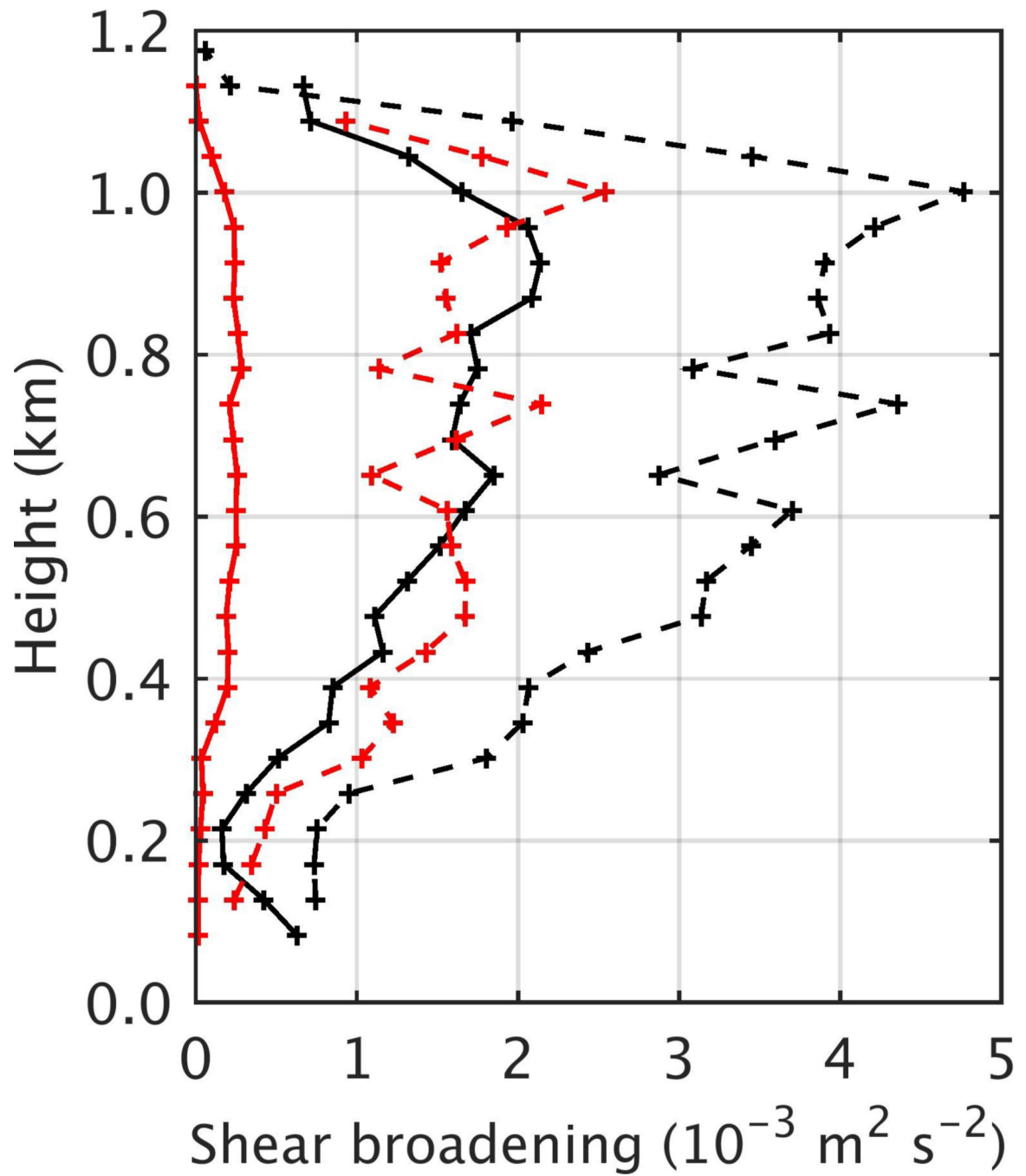
Figure 7.
Layer-mean shear broadening estimated from the observed (black lines) and modified (red lines) mean Doppler velocities. The solid and dashed lines are for the horizontal and vertical shear broadening terms, respectively.
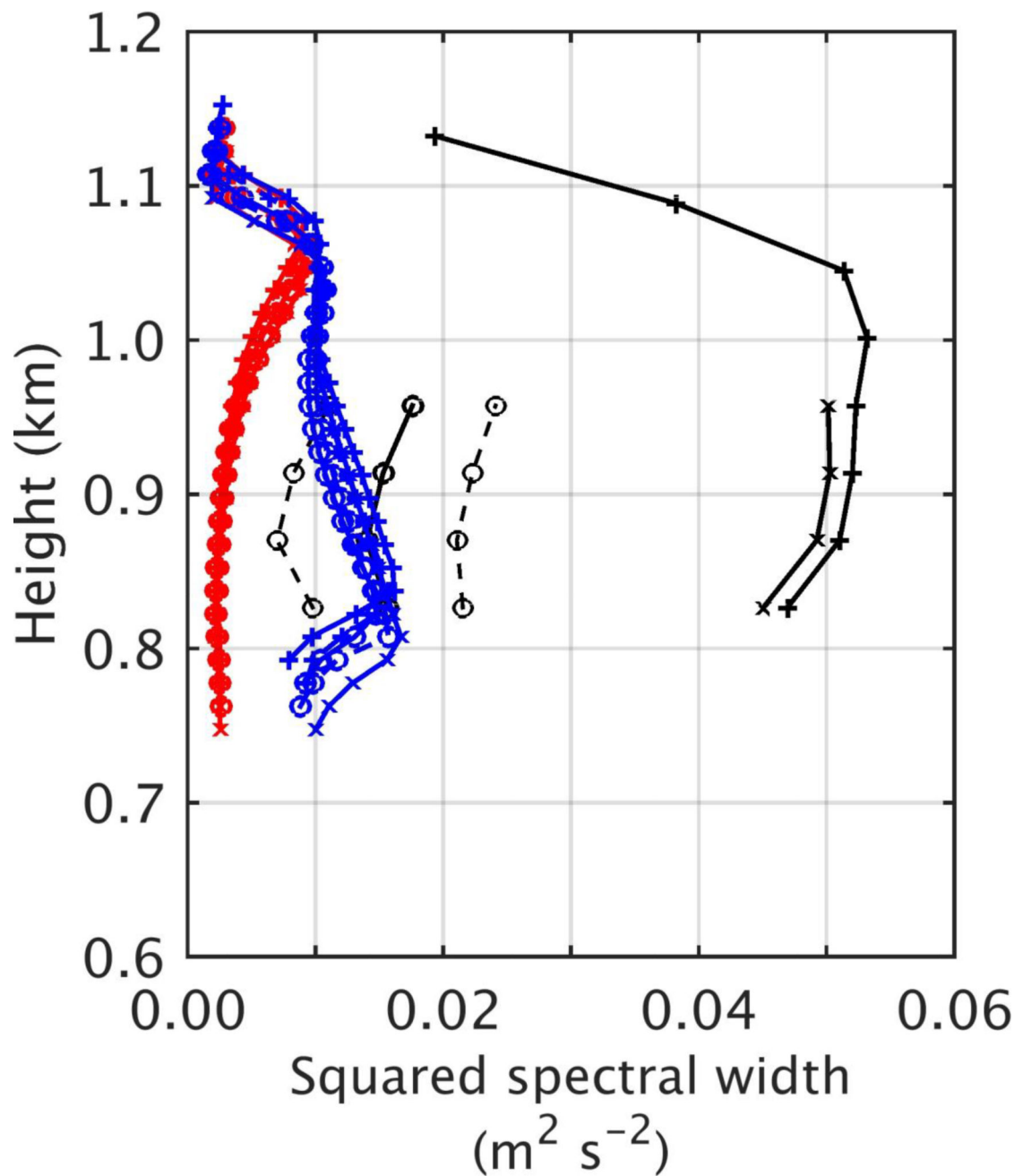
Figure 8.
Profiles of the observed squared spectral widths (black solid line with "+"), observed
squared spectral widths with shear broadening removed (black solid line with "×"), retrieved
microphysical broadening (black solid line with "○") and its uncertainty range (thin black
dashed lines with "○"). In addition, red lines represent the model microphysical broadening
at the five time slices of the LOW simulation, whereas the blue lines are from the HIGH
simulation. Profiles for DHARMA simulations are shifted up by 50 m to compensate for the
different location of liquid cloud in the simulations and observations.
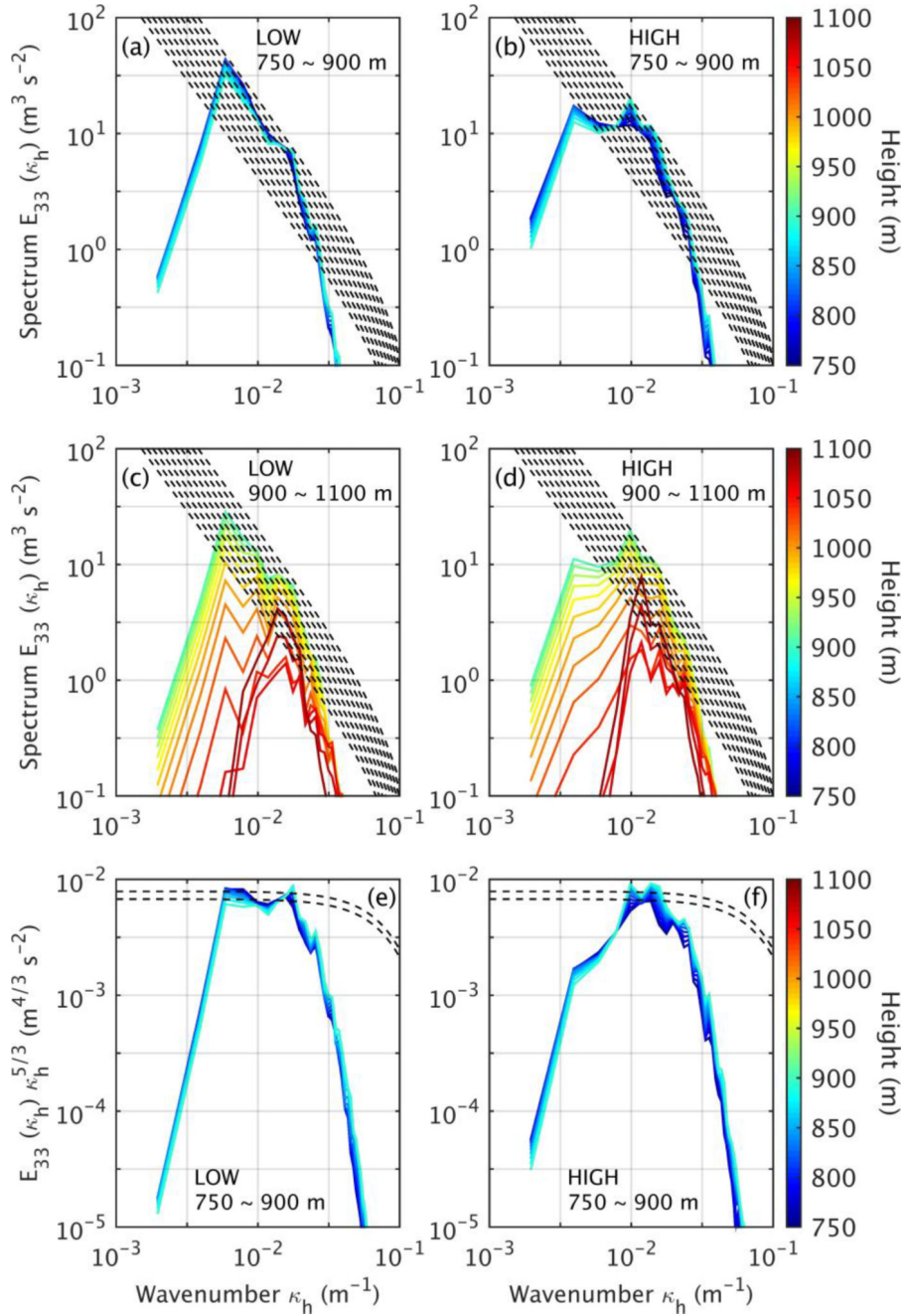
Figure 9.
Power spectra of vertical winds in the lower (first row) and upper (second row) part of the liquid cloud in the LOW (left column) and HIGH (right column) simulations. The flow fields at 4 h of both simulations were used. Black dashed lines show the theoretical spectra for dissipation rates from $10^{-4.0}$, $10^{-3.9}$, …, to $10^{-3.0}$ m^2 s^{-3} Colors of lines indicate heights of the model layers in meter. Also shown are the flattened spectra of the vertical air velocity in the lower part of the liquid cloud in the LOW simulation (third row). Black dashed lines are theoretical flattened spectra for dissipation rates of $10^{-3.1}$ and $10^{-3.2}$ $m^2 s^{-3}$, respectively, given the filter used in DHARMA.
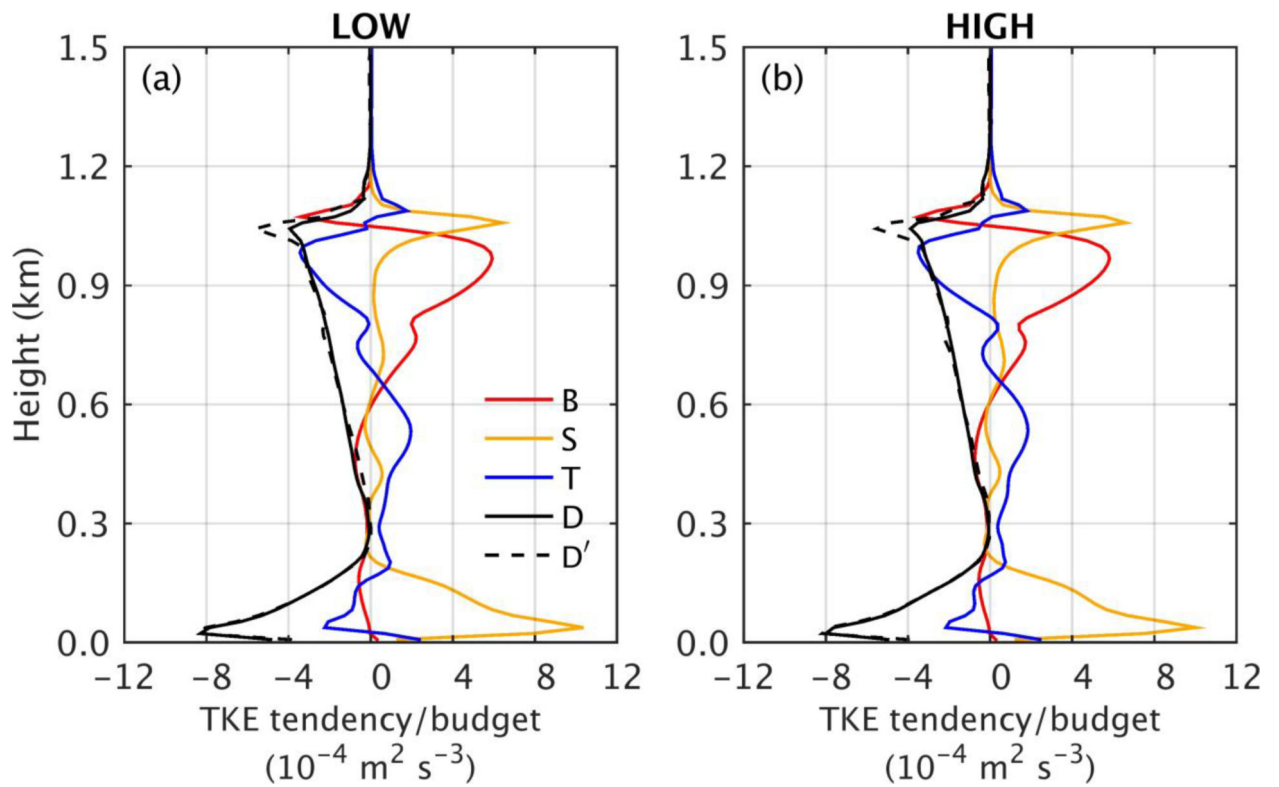
Figure 10.
Turbulent kinetic energy budgets for the LOW and HIGH simulations averaged from 2 h to 4 h. S represents shear, B buoyancy, T transport, D dissipation, and D′ the tendency required to balance the TKE tendency in the model and S, B, and T.